Earth and Planetary Science Letters 559 (2021) 116768

Contents lists available at ScienceDirect

Earth and Planetary Science Letters

www.elsevier.com/locate/epsl

Small-scale heterogeneity in the lowermost mantle beneath Alaska and northern Pacific revealed from shear-wave triplications

Yuwei Li *, Meghan S. Miller, Hrvoje Tkalčić, Malcolm Sambridge

Research School of Earth Sciences, The Australian National University, Canberra ACT 2601, Australia

ARTICLE INFO

Article history:
Received 10 June 2020
Received in revised form 10 January 2021
Accepted 16 January 2021
Available online xxxx
Editor: M. Ishii

Keywords:
lowermost mantle
non-linear inversion
waveform modelling
phase transition
small-scale chemical heterogeneities
slab debris

ABSTRACT

The D″ layer, regarded as a thermal boundary layer and a chemically distinct region above the core-mantle boundary (CMB), has been associated with the phase transition from bridgmanite (Bm) to post-perovskite (pPv) in the lowermost mantle. However, the composition of the lowermost mantle and thermal conditions where Bm-pPv phase-transition occurs is still debatable. The methods typically used to study the fine-scale seismic features in the D″ layer has provided important information. However, trial-and-error seismic waveform modelling cannot uniquely quantify D″-layer properties because of subjective model-parameterization choices and inherent non-uniqueness of solutions and the waveform inversion method has a limited resolution of the velocity gradient and depth of the D″ discontinuity. We develop a grid-search scheme to constrain the detailed 1-D shear-wave velocity structure in the lowermost mantle beneath Alaska and the northern Pacific, accompanied with quantitative assessment of the uncertainty of 1D models. Our results show strong lateral variations of the D″ discontinuity from west to east beneath Alaska, along with the existence of smaller-scale heterogeneities in the east. We find a broad velocity increase, as thick as 240 km, at the top of D″ that indicates this region may involve a composite of downwelling thermo-chemical anomalies at the CMB. There are even smaller scale heterogeneities of approximately 120 km × 120 km in size with larger lateral variations in the lowermost mantle beneath northern Pacific. Both the magnitude and gradient of the velocity at the top of the D″ layer vastly change in adjacent regions, with an increase from 2.8% to 4.5% in magnitude and from 0.08% to 1.2% in gradient, but with a relatively consistent depth of the D″ discontinuity at ~340 km above the CMB. The weak correlation between D″ topography and velocity variations indicate chemical heterogeneities must be present beneath the northern Pacific, which might come from north-westward subducted Pacific oceanic lithosphere. Our characterisation of the spatial pattern of small-scale heterogeneities in the lowermost mantle supports a hybrid thermo-chemical boundary layer (TCBL) model beneath Alaska and northern Pacific.

1. Introduction

The D″ layer, the lowermost few hundred kilometres of the mantle, is one of the most unexplored regions on the Earth's interior (e.g., Cobden and Thomas, 2013; Lay, 2015). It has been regarded as a thermal boundary layer and a chemically distinct region above the core-mantle boundary (CMB), which plays a critical role in the mantle and core convection. The top of the D″ region is characterised by a sharp change or discontinuity in seismic velocities with strong lateral variations in the depth (e.g. Lay and Helmberger, 1983; Garnero and Helmberger, 1996). This discontinuity likely stems from a phase transition from bridgmanite (Bm) to post-perovskite (pPv) under high pressure-temperature conditions (~2500 K and 125 GPa) (Murakami et al., 2004; Oganov and Ono, 2004; Hirose, 2006; Shim, 2008). Shear-wave tomographic studies have provided key information for the lowermost mantle structure as the lateral coverage and density of data increase and inversion methodologies improve (e.g., Grand, 2002; Simmons et al., 2010; Koelemeijer et al., 2016; Durand et al., 2017). On one hand, the resolution of global shear-wave tomographic methods is still limited due to the dominant low frequency content of the waveforms utilized. Some localised S-velocity tomographic models with higher frequency content have higher resolution. However, these models are still unable to resolve the detailed seismic structure in the lowermost mantle such as the gradient of velocity increase at the top of D″ due to the coarse parameterization (e.g. Borgeaud et al., 2017). On the other hand, P-wave tomographic studies could provide valuable constraints because of higher fre-

* Corresponding author.
E-mail address: yuwei.li@anu.edu.au (Y. Li).

https://doi.org/10.1016/j.epsl.2021.116768
0012-821X/

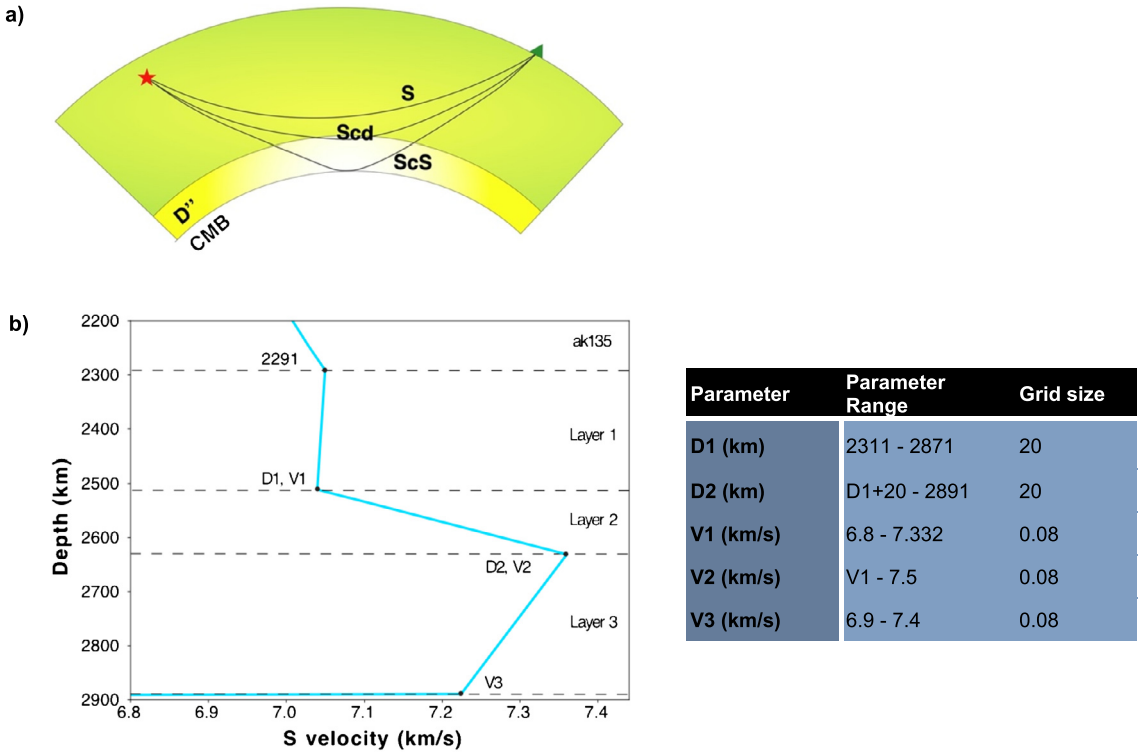

Parameter	Parameter Range	Grid size
D1 (km)	2311 - 2871	20
D2 (km)	D1+20 - 2891	20
V1 (km/s)	6.8 - 7.332	0.08
V2 (km/s)	V1 - 7.5	0.08
V3 (km/s)	6.9 - 7.4	0.08

Fig. 1. a) Raypaths of S, Scd and ScS. **b)** Model parameterisation for grid search in the D″ region inferred by previous waveform modelling results.

quency content, although the volumetric sampling of the lowermost mantle by high-frequency compressional waves (e.g. Young et al., 2013; Tkalčić et al., 2015) is somewhat inferior to the sampling by shear waves, unless long-period, P-waves diffracted around the CMB are introduced (e.g. Wysession, 1996; Hosseini et al., 2020). Therefore, waveform modelling targeting the areas where the coverage is dense uniquely provides improvements in resolution on the fine-scale seismic features in the deep interior of the Earth.

The D″ discontinuity has been broadly (albeit not globally) observed and its existence is well documented in a few regions of the lowermost mantle, including Central America (e.g. Thomas et al., 2004; Thorne et al., 2007; Ko et al., 2017), Alaska (e.g. Young and Lay, 1990; Sun et al., 2016), Central Pacific (e.g. Avants et al., 2006; Kawai and Geller, 2010), Atlantic (e.g. Yao et al., 2015; Li et al., 2019), and Siberia (Houard and Nataf, 1992; Weber and Davis, 1990). Substantial variation in the depth, sharpness and magnitude of the D″ discontinuity have been inferred (e.g. Wysession et al., 1998; Lay, 2008) using different datasets, data processing methods and selection criteria. It follows that in any given location, it is non-trivial to uniquely constrain the position and detailed seismic features of the D″ discontinuity due to the trade-offs between model parameters (e.g. Kito et al., 2007). That presents a challenge in understanding of the existence of D″ and its role in dynamic processes of the mantle and core. Is D″ caused by purely thermal processes or a combination of thermal and chemical processes? If chemical heterogeneities exist in the lowermost mantle, where do they come from? Are they associated with ancient subducted slabs?

To address some of these questions, we develop a non-linear scheme using a grid-search to map the detailed shear wave velocity structure of the D″ layer. First, we rigorously test it on synthetic data. Then we subsequently apply it to the waveform data sampling the lowermost mantle beneath Alaska and Northern Pacific, the region well sampled by the deep earthquakes from the western Pacific subduction zone recorded by seismic networks in the United States and Canada. Different characteristics in D″ have been observed beneath Alaska from west to east, transitioning from fast to slow then back to fast with different sharpness and magnitude of velocity increase (Sun et al., 2016). High-velocity anomalies with a thickness range of ∼200-400 km with a vertical resolution of 50 km have also been observed beneath the northern Pacific by Suzuki et al. (2016). Our aim is to further constrain the detailed structure at the top of D″ layer in these two regions using S-wave datasets, with a goal of investigating and obtaining a better understanding of the nature of D″.

2. Method and validation

The commonly used approach of trial-and-error seismic waveform modelling has provided important information on the fine structure of D″, however, it cannot uniquely quantify D″-layer properties because of subjective model-parameterization choices and inherent non-uniqueness of solutions. Kawai et al. (2007) developed a quantitative and objective waveform-inversion approach to provide an independent determination of the lowermost mantle structure from forward waveform modelling, while its limited constraint on the velocity gradient and depth of the D″ discontinuity impedes deciphering the composition of the lowermost mantle and thermal conditions where Bm-pPv phase-transition occurs. A method that provides quantitative and objective measurements of misfits between observations and synthetic seismograms and could resolve the detailed velocity structure at the top of the D″ is preferable for understanding the dynamics of the deep mantle. This is the rationale behind developing the grid-search algorithm presented here. We explored model parameter space for optimal 1-D shear-wave velocity models for the D″ region using the tangential component of S waveforms (S, Scd and ScS) between 70° and 85°, where the direct S wave, the core-reflected phase ScS and the triplication-related arrival Scd in between, all transverse the D″ layer within the region of our primary interest and can be best observed (Fig. 1).

2.1. Parameterization and misfit function

Grid-search methodology requires a large number of forward computations. The viability of the method depends on the number of unknowns and the efficiency of calculating synthetic seismograms. To reduce computational costs, but also ensure that the resolution of the seismic structure is high enough to constrain the velocity gradient of D″, we set the number of model parameters to five based on previous forward waveform modelling results (e.g., Li et al., 2019; Sun et al., 2016): the depths of two interfaces (D1 and D2), and the shear-wave velocity at those two interfaces (V1 and V2) and the core-mantle boundary (CMB) as V3. After rigorous synthetic tests, we chose a grid spacing of 20 km in depth and a shear velocity of 0.08 km/s for the first round of search to find the optimal model (Fig. 1b). Then we chose a grid size of 10 km in depth and shear velocity of 0.02 km/s varying close to the optimal model for the second round of grid search to refine our results. Velocities between the grid points were linearly interpolated. In total 119,364 three-layer half space models were generated (Fig. 1b). Considering the large number of forward modelling computations required, we used the efficient ray theoretic approach of Wentzel, Kramers, Brillouin, and Jeffreys, commonly known as the WKBJ method (Chapman and Orcutt, 1985) to calculate the Green's functions from 70° to 85° every 0.5° and then convolved them with a Gaussian source-time function of duration of 12 seconds to produce the synthetic waveforms. However, WKBJ might have some limitations on the accuracy of calculating seismograms near the grazing incidence angle due to the usage of frequency independent reflection-transmission coefficients. To test the plausibility of using WKBJ in this study, we compared the waveforms generated using Frequency-wavenumber method (FK) and WKBJ (Fig. S1). There are minor differences between the waveforms generated using these two methods after 81° while they share similar features in our focused distance range (70°-80°). This showed that WKBJ was adequate for the following analyses. The source-time function was chosen to correspond with the Gaussian filter used in data processing, which is illustrated in detail below.

The optimal model at the bottom of the corresponding Scd phase ray path was determined by the misfit function φ, defined as follows:

$$\varphi = \frac{\sum_{i=1}^{N_s} W_i \times \sqrt{\frac{\sum_{j=1}^{m_i}(O_{ij}-S_{ij})^2 + W_0 \times \sum_{j=m_i+1}^{k_i}(O_{ij}-S_{ij})^2 + \sum_{j=k_i+1}^{n}(O_{ij}-S_{ij})^2}{n+(W_0-1)\times(k_i-m_i)}}}{\sum_{i=1}^{N_s} W_i} \tag{1}$$

where O_{ij} and S_{ij} correspond to the observed velocity displacement and the synthetics at the i-th epicentral distance and j-th time point after normalisation. N_s is the number of stations available for each dataset and n is the number of sampling points within the misfit time window. Our length of misfit time window is 100 s, with a sampling rate of 0.2 s, resulting in $n = 501$. W_i represents the weight for i-th trace, and W_0 represents the weight for the Scd time window. m_i and k_i are the starting and ending time point of the Scd phase that is manually picked by inspection of the stacked data. It reflects the different effects of S, Scd and ScS on grid-search modelling results.

2.2. Uncertainty analyses

The misfit function above is suitable for locating best-fit velocity profiles but is not sufficient for a quantification of uncertainty in the estimated parameters. To do so we need to take account of both the observational and theoretical (or epistemic) uncertainties in the forward model and parametrization, and then propagate these into the model parameters. This requires a Likelihood function, to quantify how well any model fits the data with respect to such uncertainties. Under the assumption that the combination of all noise processes can be represented by a Gaussian likelihood function $L(m)$, we have

$$L(\boldsymbol{m}) \propto \exp[-\frac{1}{2}\sum_{i=1}^{N_s} \boldsymbol{r}_i^T \cdot \boldsymbol{C}_D^{-1} \cdot \boldsymbol{r}_i] \tag{2}$$

$\boldsymbol{r}_i$ is the misfit vector $\boldsymbol{r}_i = \boldsymbol{O}_i - \boldsymbol{S}_i$ with dimension of 501×1. C_D is the data covariance matrix, incorporating the uncertainties in the data including modelling (theory) and observation (data) errors. In order to characterize all noise processes, we estimated a data covariance matrix directly from residual seismograms, $\boldsymbol{r}_{io}$, between the observations and the predictions from the best-fit model in each region found using the grid search procedure

$$\boldsymbol{C}_D = \frac{1}{N_s}\sum_{i=1}^{N_s}(\boldsymbol{r}_{io} - \overline{\boldsymbol{r}}_{io}) \cdot (\boldsymbol{r}_{io} - \overline{\boldsymbol{r}}_{io})^T \tag{3}$$

where $\overline{\boldsymbol{r}}_{io}$ is the average residual for the ith station. This approach is similar to that described by Gouveia and Scales (1998), although here the correlation and amplitude of the best-fit model residuals are taken as representative of all noise processes. As an example of how well the estimated C_D represents the true residuals between observations and synthetic seismograms from the best-fit model, Fig. 2 shows an example for the Alaska data set, and in particular the comparison between real residuals $\boldsymbol{r}_o$ and constructed synthetic residuals $\boldsymbol{r}_o'$ which is a Gaussian random variable drawn from the multi-dimensional Gaussian in (2). The similar characteristics of real residuals and synthetic residuals in terms of amplitude and correlation length, as seen in the right-hand panel in Fig. 2, confirm that it is reasonable to represent the observed waveform discrepancies by the Gaussian Likelihood in eqn. (2). Furthermore, it shows that the calculated Covariance matrix is representative of the observed waveform residuals. This is important because all subsequent detailed model error analysis is based on this data noise distribution.

With a representative likelihood available, it then becomes possible to estimate confidence intervals, or contours, about the best-fit model, as a function of any chosen parameter or pair of parameters, using the Likelihood ratio test (Koch, 1999). For example, in 1D this is done by evaluating the quantity

$$LRT(\boldsymbol{m}_p) = -2\log(\frac{L(\boldsymbol{m}_p \mid \boldsymbol{m})}{L(\boldsymbol{m}_o)}) \tag{4}$$

as a function of a chosen parameter, say $\boldsymbol{m}_p$, through the best-fit model, where $L(\boldsymbol{m}_o)$ is the likelihood function of the best-fit model, and $L(\boldsymbol{m}_p \mid \boldsymbol{m})$ is the maximum likelihood for this value of $\boldsymbol{m}_p$ optimized over all other parameters. Since LRT can be assumed to be distributed according to a Chi-square distribution with $k = 1$ degrees of freedom, then in 1-D we can find where this value reaches any desired confidence level and hence assigned a confidence interval about the best-fit model. The same process can be applied to map out confidence contours for any pair of model parameter (with $k = 2$). This process was used to assign confidence intervals in all cases discussed below.

2.3. Synthetic tests

To validate the feasibility of using grid-search modelling (GSM) for both constraining the structure of the D″ layer and finding an optimal misfit function φ, we carried out a series of synthetic ex-

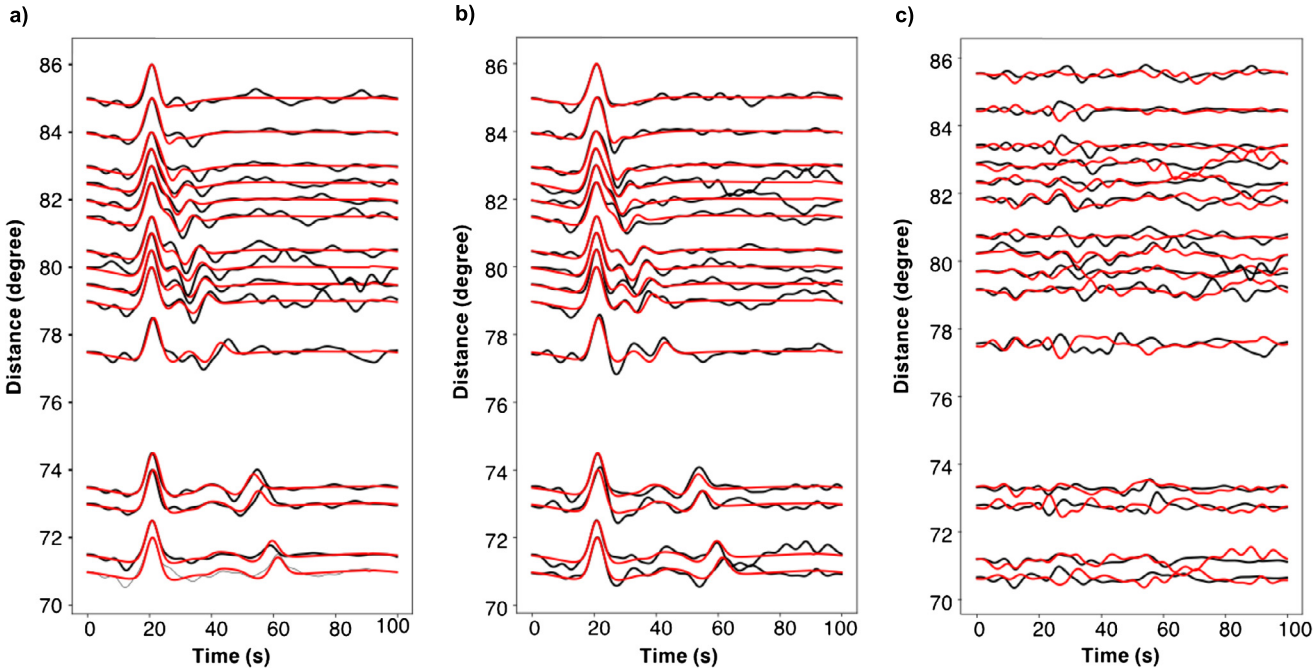

Fig. 2. a) Synthetic waveforms of the best-fit model (Red) and data (Black) for AKRegion1 (Fig. 5a). **b)** Synthetic waveforms of the best-fit model (Red) and reconstructed data $\boldsymbol{S}_i + \boldsymbol{r}_o'$ (Black). **c)** Real residuals $\boldsymbol{r}_o$ (Black) and synthetic residuals $\boldsymbol{r}_o'$ from $\boldsymbol{C}_D$ (Red). (For interpretation of the colours in the figure(s), the reader is referred to the web version of this article.)

periments with various weights, W_i and W_0, varying from 1 to 4. The input for GSM is the synthetic seismograms of a representative model of the D″ region from the previous waveform modelling study in eastern Alaska, of Sun et al. (2016) with an additional Gaussian noise with similar amplitude and correlation length of the data noise. We filtered the data to 3-50 seconds and cut the time window from −20 to 80 seconds relative to the theoretical S arrival times with a sampling rate of 0.2 s. Fig. 3 demonstrates the good recovery of input model Model 1 with GSM ($W_0 = 2$ and $W_i = 1$), especially at the top of the D″ layer. For this synthetic case we performed a Likelihood ratio test as described above (see Fig. S2). For this idealized case the uncertainties for four parameters V1, V2, D1, and D2 expressed as a confidence interval about the best-fit solution are around ±0.01 km/s, ±0.02 km/s, ±10 km and ±10 km at a 68% confidence (Fig. S2). The GSM results are less sensitive to the bottom of the D″ layer with an uncertainty of V3 at ±0.08 km/s. This could be due to the structure of the lowermost mantle is predominantly constrained by the ScS phase and the fit of ScS was influenced by the fit of Scd. Since our interest is the top of the D″ layer, we found that using GSM with $W_0 = 2$ and $W_i = 1$ is effective to constrain that parameter.

We also tested the influence of different weights for W_i at each epicentral distance range on the modelling results. The test results (Fig. S3) show that data with distances from 70° to 80° are crucial for constraining the velocity structure at the top of D″ layer, in particular the gradient and magnitude of velocity increase and the thickness of D″ layer, while the data between 80° and 85° have less impact.

3. Application of the grid-search scheme to shear-wave seismograms

After validating that it is feasible to apply GSM to constrain the D″ structure with appropriate weights W_0 and W_i through the synthetic experiments, we apply it to the waveform data sampling the lowermost mantle beneath Alaska and the northern Pacific.

Generally, tomograms of shear-wave velocity in the lowermost mantle display fast velocity patches beneath the circum-Pacific and dominant high velocity features with localized slow patches beneath the northern Pacific (Fig. 4). A recent waveform modelling study revealed a lateral variation of D″ structure beneath Alaska (Sun et al., 2016), suggesting a transition from normal mantle to upwelling then to a slab debris from west to east. However, the coverage of each waveform modelling result (west, middle and east) is broad, as large as 480 km × 720 km in size. Smaller-scale heterogeneities are also present at the core-mantle boundary (e.g. Rost and Thomas, 2010; Tkalčić et al., 2015; Yu and Garnero, 2018). To explore the potential existence of smaller-scale heterogeneities, we first applied GSM to three events to compare the consistency of our results with previous studies (Sun et al., 2016). Then we modelled the smaller-scale subregions that were grouped based on the characteristics of S wave triplications. Another area of interest is the northern Pacific, which is less studied due to the previously lack of data coverage. However, the densely spaced USArray Transportable Array across North America (EarthScope Working Group (2000)) and frequent deep earthquakes in the western Pacific subduction zone provide new data to probe the D″ structure in this region.

3.1. Data

We used the tangential component of broadband waveform data for 11 events that occurred along the western Pacific subduction zone with Mw magnitudes greater than 5.5 and depth larger than 150 km between 2010 to 2018 (Table 1) and three events from 2010 to 2013 used in Sun et al. (2016) for comparison purpose. More than 2500 traces were recorded with signal-to-noise ratios above 5. Fig. 4 shows a map of events, stations and theoretical ScS bounce points at the core mantle boundary in this study. Data was processed by removing the instrument response, filtering to 3-50 s and deconvolving its source time function obtained from the SCARDEC database (Vallée and Douet, 2016) using an iterative deconvolution method (Kikuchi and Kanamori, 1982) with a 12 s Gaussian filter. The traces sampling each region were then aligned

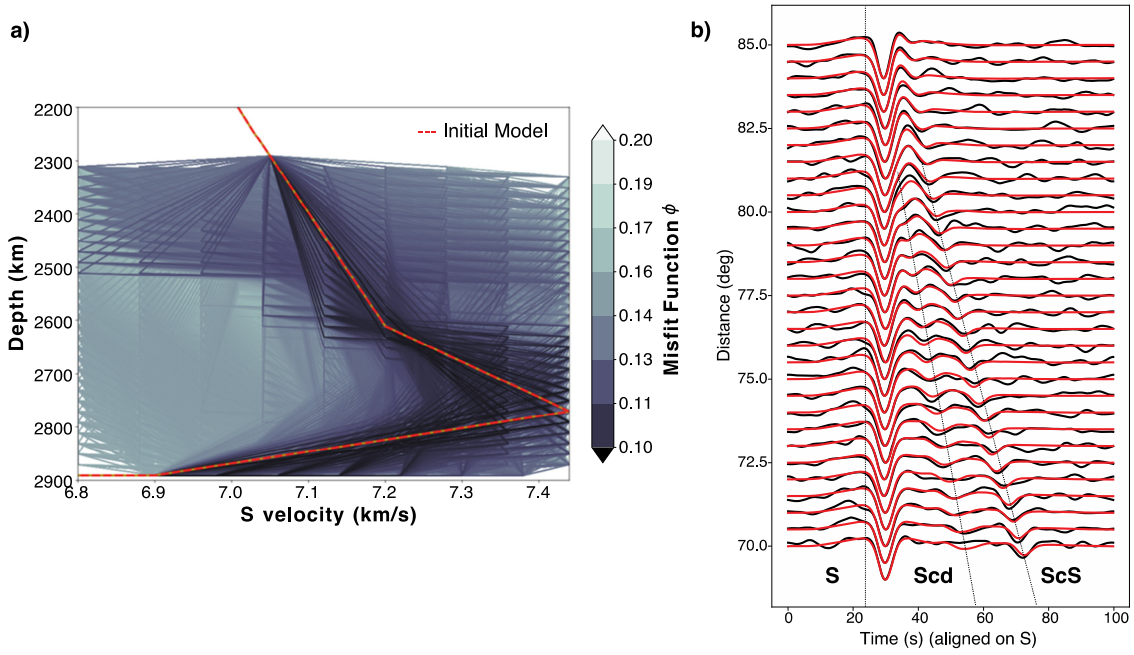

Fig. 3. a) Synthetic recovery test of GSM for a three-layer half space model (red dashed line) shown in a logarithmic colour scheme. **b)** Comparison of synthetic data and synthetic waveforms of the best-fit model (yellow line in a)). The initial model was well-recovered, demonstrating the feasibility of applying GSM to constrain the 1-D shear velocity structure in the D″ layer.

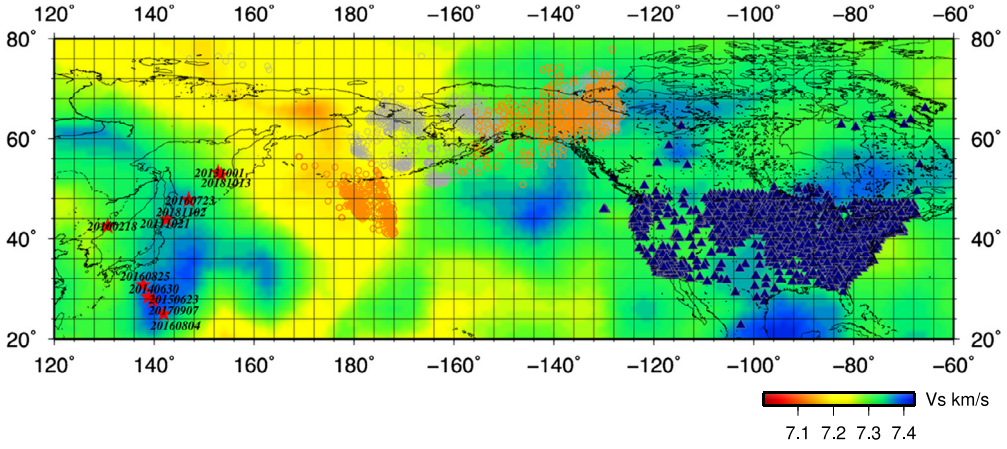

Fig. 4. Map of events (red stars), stations (blue triangles) and S turning points at the core-mantle boundary from new data in this study (orange circles) and data from Sun et al. (2016) (grey circles). The background is S wave tomography model GyPSuM at the depth of 2900 km (Simmons et al., 2010).

Table 1
Earthquakes used in this study.

Event date	Latitude (°)	Longitude (°)	Depth (km)	Mw
20100218	42.28	130.66	578	6.9
20111021	42.83	142.52	191	6.2
20131001	53.20	152.81	585	6.7
20140630	28.42	138.75	522	6.2
20150623	27.68	139.85	458	6.5
20160723	47.68	146.91	423	5.8
20160804	24.98	141.91	522	6.3
20160825	30.69	137.78	473	5.9
20170907	27.79	139.75	460	6.1
20181013	52.70	153.41	477	6.7
20181102	47.48	146.86	450	5.9

the S peaks using the adaptive alignment stacking method (Rawlinson and Kennett, 2004) and then linearly stacked every 0.5° from 70° to 85°.

4. Results: D″ structure beneath Alaska and northern Pacific

4.1. Alaska

Fig. 5b shows the D″ model from grid-search modelling using the data from previous trial-and-error waveform modelling for three separate regions (Fig. 5a) (Sun et al., 2016). We plotted the top 1000 models with the smallest $-2logL(m)$ in a logarithmic colour scheme. The trend of lateral variation in the structure of the D″ layer is consistent in these two studies, from a sharp velocity increase with moderate velocity jump in the west to a thin D″ layer with an apparent velocity increase in the middle and to a gradual velocity increase in the east. There are minor differences in the seismic features of the obtained models between two studies. The depth of D″ discontinuity in our study beneath western and eastern Alaska, at 360 km above CMB, is 80 km shallower than the result from Sun et al. (2016) (Fig. S4a). This discrepancy might be because we used different methods in the two studies. The 2-D

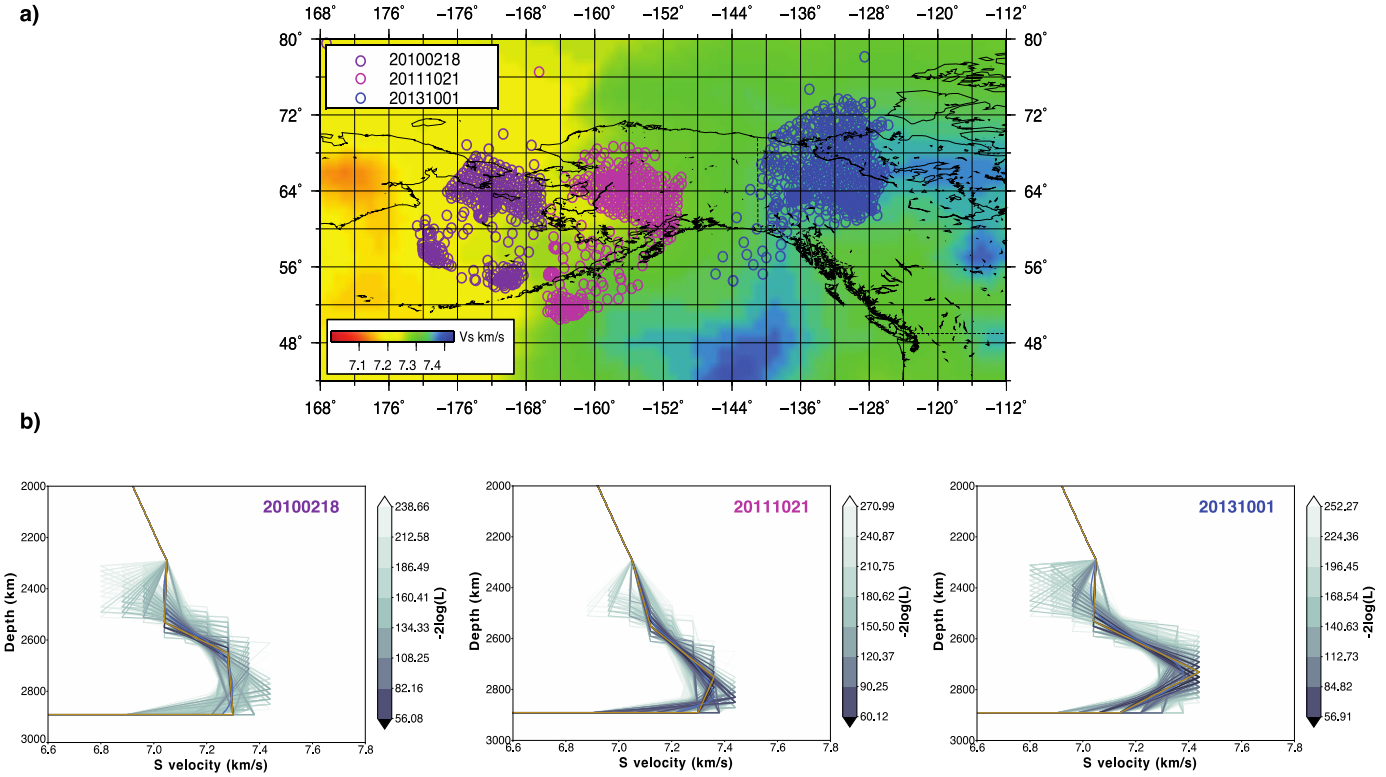

Fig. 5. a) Theoretical ScS bounce points at the core-mantle boundary for three events that were analysed by Sun et al. (2016) using forward waveform modelling. The background is S wave tomography model GyPSuM at the depth of 2900 km (Simmons et al., 2010). **b)** D″ model from grid-search modelling using the data from Sun et al. (2016). The optimal model for each region is plotted in yellow. The blue model designates the average of top 100 models.

finite difference method in Sun et al. (2016) has a better accuracy on the waveforms near the gazing incidence than WKBJ used here. Our study's different results could also be associated with the trade-off of fitting the Scd and ScS phases in the grid-search scheme. Despite the minor differences, the general velocity feature within the lowermost 280 km above CMB in the west and east of Alaska from two studies are similar. Both models have a sharp velocity increase from 7.2 to 7.3 km/s at a depth of 280 km above CMB in the west and a gradual velocity increase at the top of D″ layer from 7.2 to 7.4 km/s across 180 km, followed by a gradual velocity decrease from 7.4 to 6.9 km/s at CMB across 100 km in the east. This consistency not only demonstrates that our method is viable and effective, but also displays the increasing heterogeneity of fast slab-related material at the core-mantle boundary.

Previous waveform modelling provides first-order information on the D″ velocity structure (e.g. Lay, 2008; Sun et al., 2016; Li et al., 2019). However, as mentioned above, the sampling area for each representative 1-D velocity model is broad, covering near 480 km × 720 km in size at the CMB. Smaller-scale heterogeneities may exist within the region. To probe possible smaller-scale heterogeneities at CMB, we applied GSM to data sampling each subregion, as small as 2° × 2° in size (120 km × 120 km at the CMB) that were grouped based on the behaviour of shear wave triplications beneath eastern Alaska.

Five subregions beneath Alaska, AKRegion1 to AKRegion5, are marked in different colours in Fig. 6a, with 49, 116, 11, 38, and 9 sampling points respectively. Distinct characteristics of Scd and ScS were observed in different regions, such as the differential travel times $T_{Scd\text{-}S}$ and $T_{ScS\text{-}S}$, and relative amplitudes: A_{Scd}/A_S and A_{ScS}/A_S. For example, Scd and ScS arrive later for AKRegion4 compared with AKRegion3 (Fig. 6d). The amplitude ratio, A_{Scd}/A_S and A_{ScS}/A_S sampling AKRegion4 are also smaller. These features are well reflected in the GSM results (Fig. 6c), suggesting a smaller velocity increase from 7.12 km/s to 7.36 km/s within a thinner transition zone (160 km) at the top of D″ layer in AKRegion4 in comparison with the other three regions. The D″ velocity models for AKRegion1, AKRegion2, and AKRegion3 are similar at the top of D″ layer, which have shear velocity increase from 7.12 km/s to 7.44 km/s within the top 240 km of D″ layer with a variance of 20 km in depth. However, they have different magnitude and sharpness of velocity reduction at the bottom. We did not intend to interpret this difference here because the sensitivity of GSM to the lowermost low-velocity layer at CMB is still limited. For AKRegion5, there is a lack of data coverage between 70° to 80°, hence the structure of D″ layer in this region was not well resolved (Fig. S5).

The uncertainty of each parameter is within reasonable range from our 1D and 2D likelihood ratio test results. Fig. 7 shows the 1D likelihood ratio test for five parameters and smoothed 2D likelihood ratio test for each parameter pair in AKRegion1. The original 2D likelihood ratio test result without linear interpolation is shown in Fig. S6. The uncertainty for shear wave velocity at the top of the D″ layer (V1) is about ±0.02 km/s, and the uncertainty of the depth of the D″ discontinuity (D1) expressed as a confidence interval about the best-fit solution is about 10-15 km at a 68% confidence. However, because of the non-linearity of the problem, the best-fit solution does not necessarily lie in the centre of the confidence intervals. Typically, the upper bound is between 10-15 km higher than the best-fit solution, while the lower bound is between 10-15 km lower than the best-fit solution. Similar statements can be made for other levels of confidence. V2 and D2 have slightly larger uncertainties than V1 and D1, at ±0.04-0.08 km/s and 20 km at a 68% confidence. The lowermost part of the D″ layer structure is less constrained, which is shown from the larger uncertainties of V3, at ±0.08-0.16 km/s at a 68% confidence. This could be due to the complexities at the core-mantle boundary or potentially the limited resolution of the dataset. The uncertainties for other regions can be found in the supplementary material (Fig. S7-S9). In general, the shear wave velocity structure at the top of D″ layer

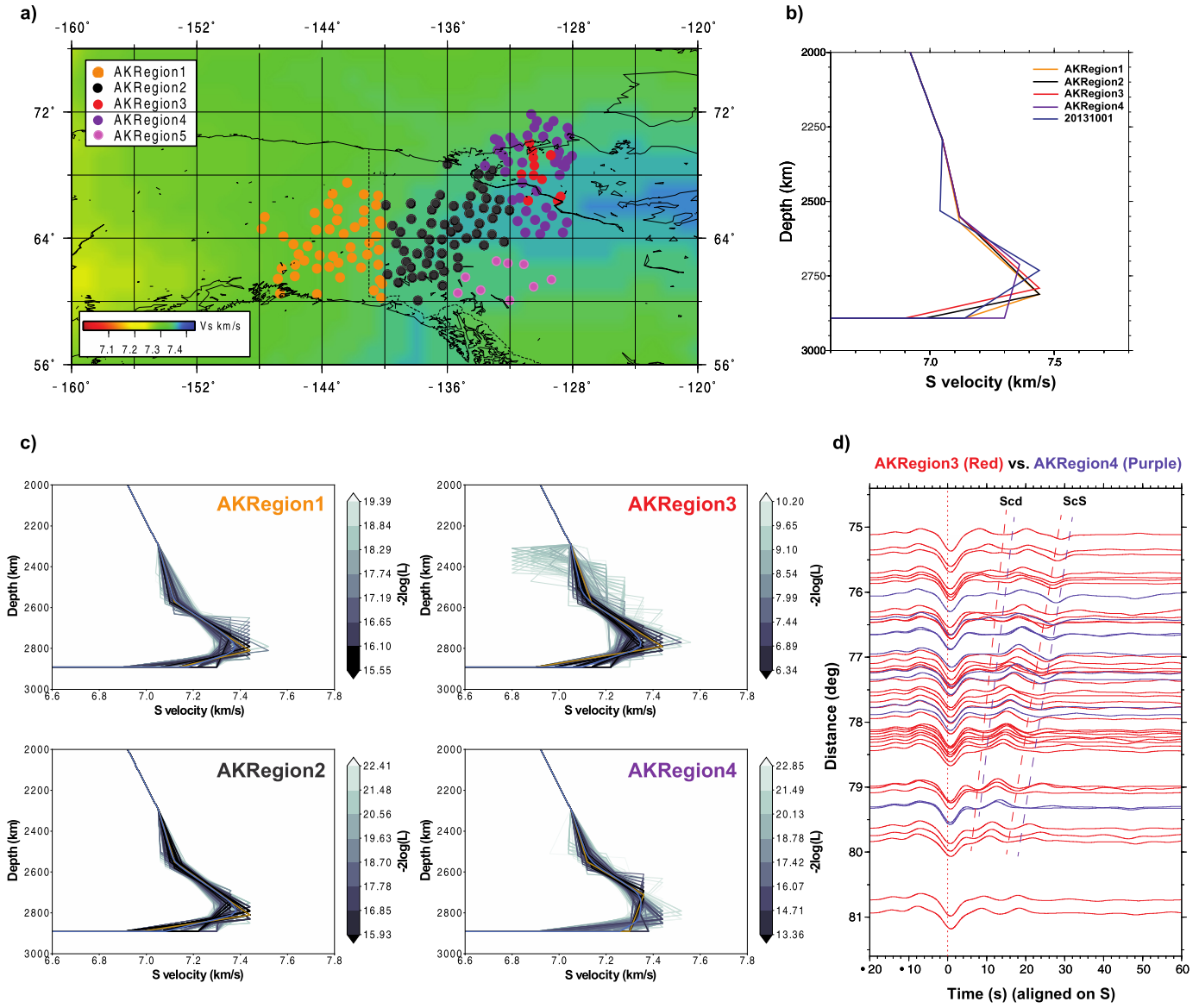

Fig. 6. a) Theoretical ScS bounce points for data sampling the lowermost mantle beneath eastern Alaska. **b)** GSM optimal 1-D velocity models for each subregion. **c)** Grid-search modelling results for each subregion (Yellow represents the optimal model and the blue represents the average of top 1000 models). **d)** Comparison of tangential component of seismic records for AKRegion3 (red lines) and AKRegion4 (purple lines), showing different characteristics of Scd and ScS both in amplitude and arrival time.

is resolved very well. The 2D likelihood ratio tests provides further support for the high-resolution of the top of D″ layer seen in the grid search solutions. The parameters of the optimal model for each subregion locate within the area of the high likelihood ratios, where there is larger goodness of fit between synthetics and data.

From our GSM results, we could observe small lateral variations in the magnitude and sharpness of the velocity gradient at the top of D″ region beneath eastern Alaska, suggesting the existence of smaller-scale heterogeneities in our sampling region.

4.2. Northern Pacific

As with the data sampling beneath Alaska, we applied GSM to four subregions, NPRegion1, NPRegion2, NPRegion3 and NPRegion4 beneath northern Pacific (Fig. 8a), with 17, 30, 32, and 30 traces sampling each region, respectively. These four subregions were divided based on the general observation of the S-wave phases (S, Scd and ScS) sampling the deep mantle. Different characteristics of Scd and ScS were observed in different regions. For example, Fig. 8c shows the comparison of tangential components of shear waveforms for NPRegion3 and NPRegion4. The differential travel times $T_{Scd\text{-}S}$, $T_{ScS\text{-}S}$ for NPRegion3 are larger and relative amplitudes A_{Scd}/A_S is smaller comparing with NPRegion4. The velocity structure in the lowermost mantle was well constrained for NPRegion1, NPRegion2, NPRegion3 and NPRegion4.

Large variations in sharpness and magnitude of the velocity gradient at both the top and bottom of the D″ layer was observed from northwest to southeast beneath the northern Pacific (Fig. 8b). The magnitude of the velocity increase at the top of the D″ layer increases from northwest to southeast, from 7.12 km/s to 7.28 km/s in NPRegion1 and NPRegion2, from 7.04 km/s to 7.28 km/s in NPRegion3, and from 7.12 km/s to 7.44 km/s in NPRegion4. The depth of the D″ discontinuity is similar among all subregions, with 20 km difference between NPRegion1, NPRegion3 (340 km) and NPRegion2, NPRegion4 (360 km). However, a large variation in the velocity gradient ($(V2 - V1)/(D2 - D1) \times 100\%$) at the top of D″ from NPRegion1 to NPRegion4 was observed, from 0.2%, 0.08%, 1.2% to 0.16%.

The uncertainties of GSM obtained parameters are generally larger in the northern Pacific than for Alaska by a factor of 6

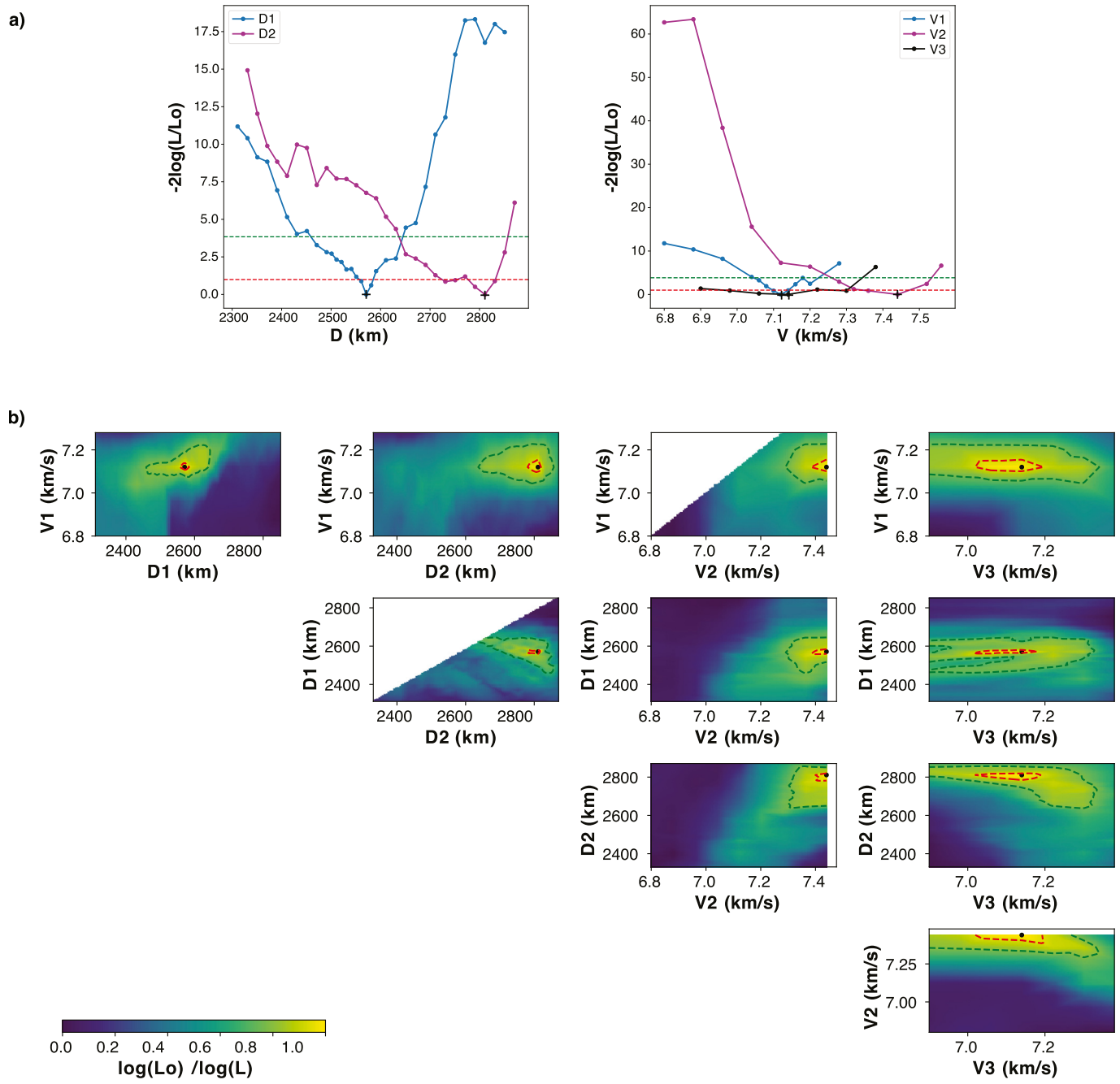

Fig. 7. a) 1D Likelihood ratio tests of five parameters, V1, V2, D1, D2, D3, for AKRegion1. The parameters for optimal model are plotted in black cross, along with the critical value of chi-square distribution at 68% confidence (red dashed lines) and 95% confidence (green dashed lines). **b)** Smoothed 2D Likelihood ratio tests of 10 parameter pairs. Parameters for the optimal model are plotted in black dots, along with the contours at a confidence level of 68% (red dashed lines) and 95% (green dashed lines).

(Fig. S10-S13), which may be due to both observational and theoretical errors. The theoretical errors here could come from imperfections such as the ray theory approximation, the inability of 1D models to account for the existence of complex structures and anisotropy, or any processing and model parametrization effects. However, there is a good fit between synthetics of the representing model from grid search and seismic records for each subregion. Fig. 8d are two examples of the comparison between the synthetics of the optimal model and data for NPRegion3 and NPRegion4.

Our GSM results suggest fine-scale heterogeneities exist in the lowermost mantle beneath northern Pacific, with a sharp velocity contrast between adjacent areas. The shear wave velocity profile of the D″ layer beneath northern Pacific is likely to be more complicated than that beneath Alaska.

5. Discussion and a way forward

In this study, we used a grid-search method to explore a more complete model parameter space for shear-wave velocity models of the lowermost mantle than the commonly used waveform modelling methods (e.g. Lay, 2008, 2015; Sun et al., 2016). We identified small-scale heterogeneities of approximately 120 km × 120 km in size in the lowermost mantle beneath Alaska (Fig. 6a) and northern Pacific (Fig. 8a).

We found that the shear velocity at the top of D″ layer is slightly faster towards eastern Alaska and northwestern Canada, which is consistent with previous shear-wave tomography models (e.g., Grand, 2002; Simmons et al., 2010; Koelemeijer et al., 2016), while the general D″ structure is similar beneath eastern

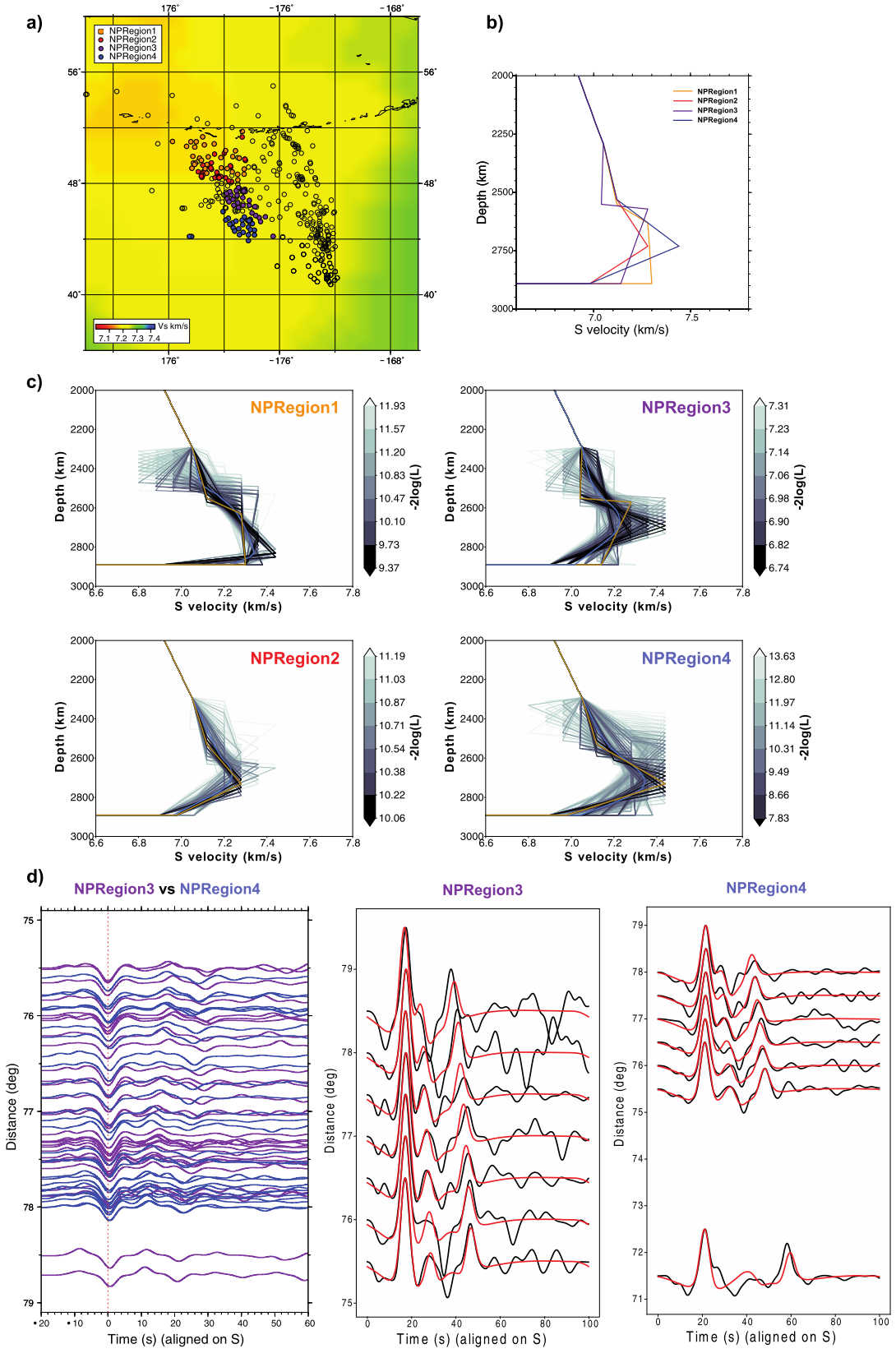

Fig. 8. a) Theoretical ScS bounce points for data sampling the lowermost mantle beneath northern Pacific. Black circles represent the data fulfilled the initial selection criteria but either not in the target region or with abnormal waveforms not suitable for modelling. **b)** GSM optimal 1-D velocity models for each subregion. **c)** Top 1000 grid-search modelling results for each subregion. (Yellow represents the optimal model and the blue represents the average of top 1000 models). **d)** (Left) Comparison of tangential component of seismic records for AKRegion3 (purple lines) and AKRegion4 (blue lines). (Right) Comparison of the synthetics (red) of the representing model with data (black) for NPRegion3 and NPRegion4.

Alaska from west to east (AKRegion1, 2, 3). This broad velocity increase layer in AKRegion1, AKRegion2, and AKRegion3, as thick as 240 km, at the top of the D″ layer can be explained by the phase transition from bridgmanite (Bm) to post-perovskite (pPv) within slab debris that reached the CMB.

The lateral variation in the velocity of the D″ region is larger beneath northern Pacific than beneath Alaska. Both the magnitude and gradient of the velocity increase at the top of D″ layer change vastly in adjacent regions, from 2.8% to 4.5% in magnitude and from 0.08% to 1.2% in terms of the gradient, but with a relatively consistent depth of the D″ discontinuity: ∼340 km above CMB. This observed lateral variation in the velocity of the lowermost mantle is generally consistent with the results from tomography (e.g., Simmons et al., 2010), where NPRegion1, NPRegion2 are in low-velocity region, and NPRegion4 is in higher-velocity area. However, this comparison should be considered with caution, since tomography models represent the average velocity of lowermost few hundred kilometres of the mantle while our results constrain the detailed seismic structure in the lowermost mantle with a depth interval of 20 km. This difference was reflected from our result for NPRegion3, where our model characterizes a larger velocity increase at the top of D″ but a lower average velocity comparing with NPRegion1 and NPRegion2, and the tomography model shows a higher average velocity.

The phase transition from lower-mantle MgSiO3-bridgmanite to post-perovskite can cause a sharp increase in shear wave velocity (Murakami et al., 2004; Oganov and Ono, 2004; Tsuchiya et al., 2004), which is consistent with our observations in NPRegion3. However, the broad phase transition layer for NPRegion1, NPRegion2 and NPRegion4 suggests chemical heterogeneities must be present. The observations of a relatively constant depth of the D″ discontinuity further support that chemical heterogeneities are required to explain such localized D″ features. Pure thermal effects in the lowermost mantle will produce a strong correlation between the topography of the D″ discontinuity and underlying velocity anomaly due to the change in P-T condition of the Bm-pPv phase transition, such as in the D″ layer beneath Central America (Ko et al., 2017). This lack of correlation between the height of the D″ discontinuity and velocity anomalies beneath the northern Pacific suggest a different subduction history in this region, where there could be a smaller amount of accumulated slab material at the CMB rather than a continuous subducted slab with a long history. This could suggest different mantle convection styles in different regions of the Earth.

Recent theoretical and experimental studies demonstrate that Fe and Al have significant influence on the depth and sharpness of the Bm-pPv boundary (Akber-Knutson et al., 2005; Caracas and Cohen, 2008; Ohta et al., 2008; Tsuchiya and Tsuchiya, 2006). The results from Sun et al. (2018) show that the combined effect of iron and aluminium could produce a broad transition region as thick as 410 km at 2200 K, and only regions depleted in Fe and Al near cold slabs would produce a sharp D″ discontinuity.

Our study region sits in the north of the circum-Pacific belt, where the north-westward-moving Pacific plate subducts beneath the Aleutian Island arc. If part of the Pacific oceanic lithosphere sinks into the lowermost mantle and accumulates at the CMB, there would be an abundance of Fe and Al in the D″ region from mid-ocean ridge basaltic (MORB) (Hirose et al., 2005). Hence, Bm-pPv phase transition in the lowermost mantle with the involvement of MORB bulk composition provides a probable explanation for our observations of a broad velocity-transition layer at the top of D″ in NPRegion1, NPRegion2 and NPRegion4, while the relative sharp velocity increase beneath NPRegion3 likely represents normal pyrolite mantle depleted in Fe and Al.

Our set of 1D models provide a first-order physical understanding of the lowermost mantle beneath Alaska and the northern Pacific. The observed small-scale chemical heterogeneities beneath Alaska and the northern Pacific suggest small accumulated slabs exist at the CMB of these two regions however, there are differing subducting history from the Caribbean (e.g. Ko et al., 2017). We recognize that the Fresnel zone of our seismic probe of the lowermost mantle is wider than the retrieved scale of heterogeneity, which might have resolution limit of recovering the full image and all details of the heterogeneity. However, there is a good lateral data coverage, with the spacing of D″ sampling points narrower than the Fresnel zones. This enables us to observe sharp transition that occurs between smaller-scale heterogeneities or between heterogeneity and the ambient mantle, although we acknowledge that some unmodelled effects such as source-side heterogeneity may exist. For smoother lateral variations of the D″ structure beneath Alaska, the D″ structure could be well resolved with small uncertainties in this region. However, three-dimensional effects caused by the sharp transition of the velocity features at the top of D″ layer may be present beneath the northern Pacific, which could partially account for the larger uncertainties in the likelihood ratio test results. Thus, our 1D models can be viewed as the first step towards more complete understanding the structure beneath the northern Pacific.

6. Conclusions

In summary, we present a promising way of modelling the detailed velocity structure in the lowermost mantle using a grid search for elastic parameters accompanied with quantitative assessment of the uncertainty of 1D models. Our characterisation of the spatial pattern of small-scale heterogeneities in the lowermost mantle beneath Alaska and northern Pacific suggests the D″ layer in these regions may be a partially mixed boundary layer involving a composite of downwelling thermo-chemical anomalies, a hybrid thermo-chemical boundary layer (TCBL) model proposed by Lay and Garnero (2004). Candidate materials include oceanic lithospheric slabs or eclogitic oceanic crustal components with ancient, dense chemical anomalies, dynamically concentrated into large agglomerations beneath upwellings. The D″ layer in the rest of the lowermost mantle is likely to share similar features, however, no conclusion can be made before further investigations of each region. Applying our approach to other regions of the lowermost mantle will help us validate this hypothesis, probe the origin of D″ layer and provide crucial information on the composition and the dynamics of the mantle.

CRediT authorship contribution statement

Yuwei Li: Conceptualization, Formal analysis, Methodology, Software, Visualization, Writing – original draft, Writing – review & editing. **Meghan S. Miller:** Funding acquisition, Supervision, Writing – review & editing. **Hrvoje Tkalčić:** Conceptualization, Methodology, Writing – review & editing. **Malcolm Sambridge:** Methodology, Writing – review & editing.

Declaration of competing interest

The authors declare that they have no known competing financial interests or personal relationships that could have appeared to influence the work reported in this paper.

Acknowledgements

Data were provided by IRIS Data Center. M.S.M. and Y.L. were supported by the funding from the National Science Foundation Geophysics Program under EAR-1345015.

Appendix A. Supplementary material

Supplementary material related to this article can be found online at https://doi.org/10.1016/j.epsl.2021.116768.

References

Akber-Knutson, S., Steinle-Neumann, G., Asimow, P.D., 2005. Effect of Al on the sharpness of the MgSiO3 perovskite to post-perovskite phase transition. Geophys. Res. Lett. 32.

Avants, M., Lay, T., Russell, S.A., Garnero, E.J., 2006. Shear velocity variation within the D″ region beneath the central Pacific. J. Geophys. Res., Solid Earth 111.

Borgeaud, A.F., Kawai, K., Konishi, K., Geller, R.J., 2017. Imaging paleoslabs in the D″ layer beneath Central America and the Caribbean using seismic waveform inversion. Sci. Adv. 3, e1602700.

Caracas, R., Cohen, R., 2008. Ferrous iron in post-perovskite from first-principles calculations. Phys. Earth Planet. Inter. 168, 147–152.

Chapman, C., Orcutt, J., 1985. The computation of body wave synthetic seismograms in laterally homogeneous media. Rev. Geophys. 23, 105–163.

Cobden, L., Thomas, C., 2013. The origin of D″ reflections: a systematic study of seismic array data sets. Geophys. J. Int. 194, 1091–1118.

Durand, S., Debayle, E., Ricard, Y., Zaroli, C., Lambotte, S., 2017. Confirmation of a change in the global shear velocity pattern at around 1000 km depth. Geophys. J. Int. 211, 1628–1639.

Garnero, E.J., Helmberger, D.V., 1996. Seismic detection of a thin laterally varying boundary layer at the base of the mantle beneath the central-Pacific. Geophys. Res. Lett. 23, 977–980.

Gouveia, W.P., Scales, J.A., 1998. Bayesian seismic waveform inversion: parameter estimation and uncertainty analysis. J. Geophys. Res., Solid Earth 103, 2759–2779.

Grand, S.P., 2002. Mantle shear–wave tomography and the fate of subducted slabs. Philos. Trans. R. Soc. Lond. A, Math. Phys. Eng. Sci. 360, 2475–2491.

Group, E.W., 2000. EarthScope: a look into our continent. Eos Trans. AGU 81, 122. https://doi.org/10.1029/00eo00079.

Hirose, K., 2006. Postperovskite phase transition and its geophysical implications. Rev. Geophys. 44.

Hirose, K., Takafuji, N., Sata, N., Ohishi, Y., 2005. Phase transition and density of subducted MORB crust in the lower mantle. Earth Planet. Sci. Lett. 237, 239–251.

Hosseini, K., Sigloch, K., Tsekhmistrenko, M., Zaheri, A., Nissen-Meyer, T., Igel, H., 2020. Global mantle structure from multifrequency tomography using P, PP and P-diffracted waves. Geophys. J. Int. 220, 96–141.

Houard, S., Nataf, H.-C., 1992. Further evidence for the 'Lay discontinuity' beneath northern Siberia and the North Atlantic from short-period P-waves recorded in France. Phys. Earth Planet. Inter. 72, 264–275.

Kawai, K., Geller, R.J., 2010. Waveform inversion for localized seismic structure and an application to D″ structure beneath the Pacific. J. Geophys. Res., Solid Earth 115.

Kawai, K., Takeuchi, N., Geller, R.J., Fuji, N., 2007. Possible evidence for a double crossing phase transition in D″ beneath Central America from inversion of seismic waveforms. Geophys. Res. Lett. 34.

Kikuchi, M., Kanamori, H., 1982. Inversion of complex body waves. Bull. Seismol. Soc. Am. 72, 491–506.

Kito, T., Rost, S., Thomas, C., Garnero, E.J., 2007. New insights into the P- and S-wave velocity structure of the D″ discontinuity beneath the Cocos plate. Geophys. J. Int. 169, 631–645.

Ko, J.Y.-T., Hung, S.-H., Kuo, B.-Y., Zhao, L., 2017. Seismic evidence for the depression of the D″ discontinuity beneath the Caribbean: implication for slab heating from the Earth's core. Earth Planet. Sci. Lett. 467, 128–137.

Koch, K.-R., 1999. Parameter Estimation and Hypothesis Testing in Linear Models. Springer Science & Business Media.

Koelemeijer, P., Ritsema, J., Deuss, A., Van Heijst, H.-J., 2016. SP12RTS: a degree-12 model of shear- and compressional-wave velocity for Earth's mantle. Geophys. J. Int. 204, 1024–1039.

Lay, T., 2008. Sharpness of the D″ discontinuity beneath the Cocos Plate: implications for the perovskite to post-perovskite phase transition. Geophys. Res. Lett. 35.

Lay, T., 2015. Deep Earth structure: lower mantle and D″. In: Schubert, G. (Ed.), Treatise on Geophysics, 2nd edition. Elsevier, Oxford, pp. 683–723.

Lay, T., Garnero, E.J., 2004. Core-mantle boundary structures and processes. In: The State of the Planet: Frontiers and Challenges in Geophysics, vol. 19, pp. 25–41.

Lay, T., Helmberger, D.V., 1983. A lower mantle S-wave triplication and the shear velocity structure of D″. Geophys. J. R. Astron. Soc. 75, 799–837.

Li, Y., Miller, M.S., Sun, D., 2019. Seismic imaging the D″ region beneath the Central Atlantic. Phys. Earth Planet. Inter. 292, 76–86.

Murakami, M., Hirose, K., Kawamura, K., Sata, N., Ohishi, Y., 2004. Post-perovskite phase transition in MgSiO3. Science 304, 855–858.

Oganov, A.R., Ono, S., 2004. Theoretical and experimental evidence for a post-perovskite phase of MgSiO3 in Earth's D″ layer. Nature 430, 445.

Ohta, K., Hirose, K., Lay, T., Sata, N., Ohishi, Y., 2008. Phase transitions in pyrolite and MORB at lowermost mantle conditions: implications for a MORB-rich pile above the core–mantle boundary. Earth Planet. Sci. Lett. 267, 107–117.

Rawlinson, N., Kennett, B.L., 2004. Rapid estimation of relative and absolute delay times across a network by adaptive stacking. Geophys. J. Int. 157, 332–340.

Rost, S., Thomas, C., 2010. High resolution CMB imaging from migration of short-period core reflected phases. Phys. Earth Planet. Inter. 183, 143–150.

Shim, S.-H., 2008. The postperovskite transition. Annu. Rev. Earth Planet. Sci. 36, 569–599.

Simmons, N.A., Forte, A.M., Boschi, L., Grand, S.P., 2010. GyPSuM: a joint tomographic model of mantle density and seismic wave speeds. J. Geophys. Res., Solid Earth 115.

Sun, D., Helmberger, D., Miller, M.S., Jackson, J.M., 2016. Major disruption of D″ beneath Alaska. J. Geophys. Res., Solid Earth 121, 3534–3556.

Sun, N., Wei, W., Han, S., Song, J., Li, X., Duan, Y., Prakapenka, V.B., Mao, Z., 2018. Phase transition and thermal equations of state of (Fe, Al)-bridgmanite and post-perovskite: implication for the chemical heterogeneity at the lowermost mantle. Earth Planet. Sci. Lett. 490, 161–169.

Suzuki, Y., Kawai, K., Geller, R.J., Borgeaud, A.F., Konishi, K., 2016. Waveform inversion for 3-D S-velocity structure of D″ beneath the Northern Pacific: possible evidence for a remnant slab and a passive plume. Earth Planets Space 68, 1–8.

Thomas, C., Garnero, E.J., Lay, T., 2004. High-resolution imaging of lowermost mantle structure under the Cocos Plate. J. Geophys. Res., Solid Earth 109.

Thorne, M.S., Lay, T., Garnero, E.J., Jahnke, G., Igel, H., 2007. Seismic imaging of the laterally varying D″ region beneath the Cocos Plate. Geophys. J. Int. 170, 635–648.

Tkalčić, H., Young, M., Muir, J.B., Davies, D.R., Mattesini, M., 2015. Strong, multi-scale heterogeneity in Earth's lowermost mantle. Sci. Rep. 5, 18416.

Tsuchiya, T., Tsuchiya, J., 2006. Effect of impurity on the elasticity of perovskite and postperovskite: velocity contrast across the postperovskite transition in (Mg, Fe, Al) (Si, Al) O3. Geophys. Res. Lett. 33.

Tsuchiya, T., Tsuchiya, J., Umemoto, K., Wentzcovitch, R.M., 2004. Phase transition in MgSiO3 perovskite in the Earth's lower mantle. Earth Planet. Sci. Lett. 224, 241–248.

Vallée, M., Douet, V., 2016. A new database of source time functions (STFs) extracted from the SCARDEC method. Phys. Earth Planet. Inter. 257, 149–157.

Weber, M., Davis, J., 1990. Evidence of a laterally variable lower mantle structure from P- and S-waves. Geophys. J. Int. 102, 231–255.

Wysession, M.E., 1996. Large-scale structure at the core–mantle boundary from diffracted waves. Nature 382, 244–248.

Wysession, M.E., Lay, T., Revenaugh, J., Williams, Q., Garnero, E.J., Jeanloz, R., Kellogg, L.H., 1998. The D″ discontinuity and its implications. In: The Core-Mantle Boundary Region, vol. 28, pp. 273–297.

Yao, Y., Whittaker, S., Thorne, M.S., 2015. D″ discontinuity structure beneath the North Atlantic from Scd observations. Geophys. Res. Lett. 42, 3793–3801.

Young, C.J., Lay, T., 1990. Multiple phase analysis of the shear velocity structure in the D″ region beneath Alaska. J. Geophys. Res., Solid Earth 95, 17385–17402.

Young, M., Tkalčić, H., Bodin, T., Sambridge, M., 2013. Global P wave tomography of Earth's lowermost mantle from partition modelling. J. Geophys. Res., Solid Earth 118, 5467–5486.

Yu, S., Garnero, E.J., 2018. Ultralow velocity zone locations: a global assessment. Geochem. Geophys. Geosyst. 19, 396–414.